# Measurement of the azimuthal dependence of cross-polarized lidar returns and its relation to optical depth

Nathalie Roy, Gilles Roy, Luc R. Bissonnette, and Jean-Robert Simard

We measure with a gated intensified CCD camera the cross-polarized backscattered light from a linearly polarized laser beam penetrating a cloud made of spherical particles. In accordance with previously published results we observe a clear azimuthal pattern in the recorded images. We show that the pattern is symmetrical, that it originates from second-order scattering, and that higher-order scattering causes blurring that increases with optical depth. We also find that the contrast in the symmetrical features can be related to measurement of the optical depth. Moreover, when the blurring contributions are identified and subtracted, the resulting pattern provides a pure second-order scattering measurement that can be used for retrieval of droplet size. © 2004 Optical Society of America

*OCIS codes:* 280.3640, 260.5430, 290.4210, 290.1090, 290.1310.

## 1. Introduction

Depolarization measurements have been applied almost from the inception of the lidar technique to the task of differentiating between atmospheric scatterers of liquid or solid phase. The principle of operation is well known and based on the simple fact that small homogenous liquid droplets suspended in air are spherical and that spherical homogenous scatterers do not depolarize the radiation at exactly 180°, whereas irregularly shaped solid particles give rise to significant depolarization. The pioneering developments of this technique are due to Schotland *et al.*,[1] Sassen,[2] Pal and Carswell,[3] and Platt.[4] To our knowledge Carswell and Pal[5] were the first to report in 1980 observations of polarization patterns in multiply scattered returns from controlled-environment clouds. They repeated these observations in atmospheric clouds in 1985.[6] Rakovic and Kattawar[7] provided in 1998 a consistent theoretical analysis of these findings: A simple model of second-order scattering from spherical particles reproduces the observed patterns quite well. In the mean time the work of Roy *et al.*[8] and Bissonnette *et al.*[9] on multiple-field-of-view (MFOV) lidar showed the advantage of exploiting the information content of multiple scattering for the retrieval of microphysical parameters of water clouds. Until now the MFOV measurements have been performed sequentially with different apertures or simultaneously with the help of a ring-segmented pin detector or with a holographic element.[10] Recent progress in the development of gated intensified charge-coupled devices (ICCDs) has made measurement of multiply scattered lidar light relatively simple.[11]

Although already observed and explained, the azimuthal dependence of multiply scattered lidar returns contains retrievable information on cloud parameters, e.g., optical depth and droplet size, that has not yet been exploited. In this paper we present measurements of the polarization patterns of the backscattered light performed with a linearly polarized laser beam penetrating a cloud of known optical depth. The azimuthally resolved MFOV measurements were recorded with a gated intensified CCD camera. An experimental relationship is established between the contrast of the symmetrical azimuthal pattern and the optical depth. Moreover we show that, using the measured scattered light at 0° and 90° with respect to the direction of laser pulse polarization, we can derive the second-order contribution to the measured multiple-scattering cross-polarized pattern.

The authors are with Defence Research and Development Canada Velcartier, 2459 Pie XI Boulevard North, Val-Belair Quebec, Canada G3J 1X5 (e-mail for N. Roy, nathalie.roy@drdc-rddc.gc.ca).

Received 26 August 2003; revised manuscript received 3 December 2003; accepted 9 February 2004.

0003-6935/04/132777-09$15.00/0

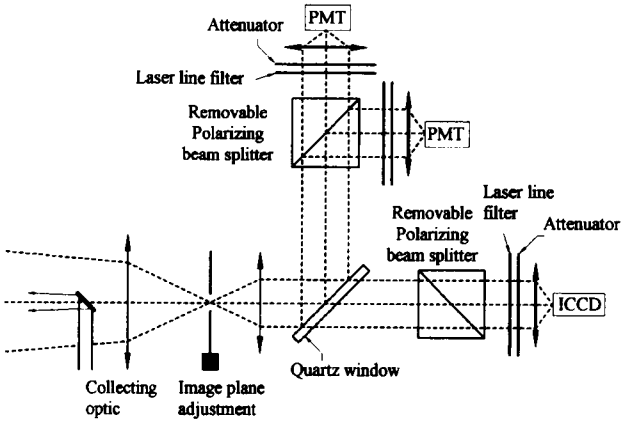


Fig. 1. Schematic of the lidar detection module including two conventional polarization channels and one channel for the measurement of the cross-polarized returns with an ICCD camera: PMT, photomultiplier tube.

## 2. Lidar System and Measurement Method

The MFOV lidar measurements were made in a 22-m-long aerosol chamber. Two dissemination systems were used to generate droplets of fairly different sizes: distributed pneumatic water nozzles and a MDG Super Max 5000 fog-oil generator. The aerosol chamber facility, the water droplet, and fog-oil clouds have been described elsewhere.[8] In short the generated water droplets are in the size range of 10–80 μm in diameter with a mean diameter near 20 μm, whereas the oil droplets have submicrometer diameters (a lognormal distribution with a geometric mean volume diameter of 0.8 μm and a geometric standard deviation of 0.58 μm). The aerosol chamber is located 100 m from the lidar. A longitudinal transmissometer is used to measure the total optical depth with a precision of 2%. The MFOV lidar measurements were made with a 100-Hz repetition-rate Nd:YAG laser (Kigre, MDL 1732 Workhorse) synchronized with a gated intensified CCD camera (Andor ICCD DH 720-18U-03). The characteristics of the outgoing laser beam are as follows: 2.5-cm diameter, 0.3-mrad divergence (50% total energy), linear polarization purity of 1/500, pulse energy in the atmosphere of 25 mJ, and pulse width of 12 ns.

Figure 1 shows the detection setup. The primary optics consists of a 200-mm-diameter off-axis parabolic mirror with a focal length of 760 mm. The position of the image plane is a function of the focal length and the object position, and it is necessary to adjust the image plane position in accordance with cloud distance. A quartz window is used to reflect part of the backscatter light on a conventional lidar polarization detection module. The transmitted light through the quartz window is collected by a polarizer cube and reimaged on the ICCD; removing the cube polarizer provides measurement of the total signal. A mask with a 1% transmission for fields of view smaller than 1.32 mrad and a 94% transmission for fields of view larger than 1.32 mrad is positioned in the image plane when required for greater dynamic range. The mask consists of a 12.5-mm-diameter, 0.5-mm-thick BK7 glass disk with 1-mm-diameter high-reflectivity (99.0%) central dot. In addition to the primary optics the lidar system is equipped with an all-weather 20-cm-diameter periscope scanner. This allows us to point the lidar in any direction. The scanner consists of a 23-cm window and three flat 30-cm-diameter mirrors set at 45°. The radial response of the whole system was characterized by a flat-field measurement performed at dusk on a clear day with the system pointing at the zenith.[12]

For the azimuthally resolved MFOV measurements we used an ICCD camera. The camera was cooled at −10 °C to reduce the dark signal and its associated shot noise. To range-resolve the recorded image, the microchannel plate intensifier was gated with a pulse generator activated by the $Q$ switch of the 100-Hz Nd:YAG laser. For each measurement event we followed a procedure that allowed us to optimize the camera acquisition speed and reduce the noise level, especially the readout noise. First, we determined the number of pulses that we need to sum on the camera chip before reading the CCD. Typically we aimed for a maximum of 20,000 counts on a pixel (the saturation level is attained at 65,535 counts) to ensure enough lidar return on the matrix of photosensors and good linearity in the camera response. Then the light background was measured just before acquiring the lidar return by opening the camera gate for the same number of times as for the lidar measurements. Finally, the background image was subtracted from the image of the lidar returns. We repeated this procedure for seven different ranges, spaced 3 m apart, to study the evolution of the lidar return with penetration depth into the aerosol chamber. With the ICCD the ranges are thus obtained sequentially while the field of views (FOVs) are obtained instantaneously. The resulting acquisition speed depends on the chosen number of pulses cumulated before the CCD camera chip is read. Typically this number was varied between 5

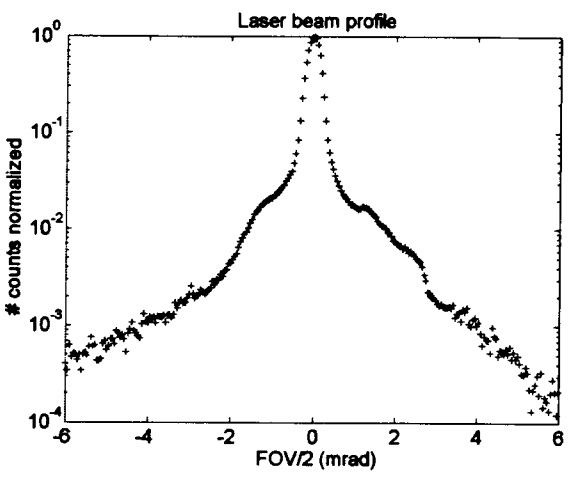


Fig. 2. Normalized intensity of the laser-beam profile as a function of FOV/2.

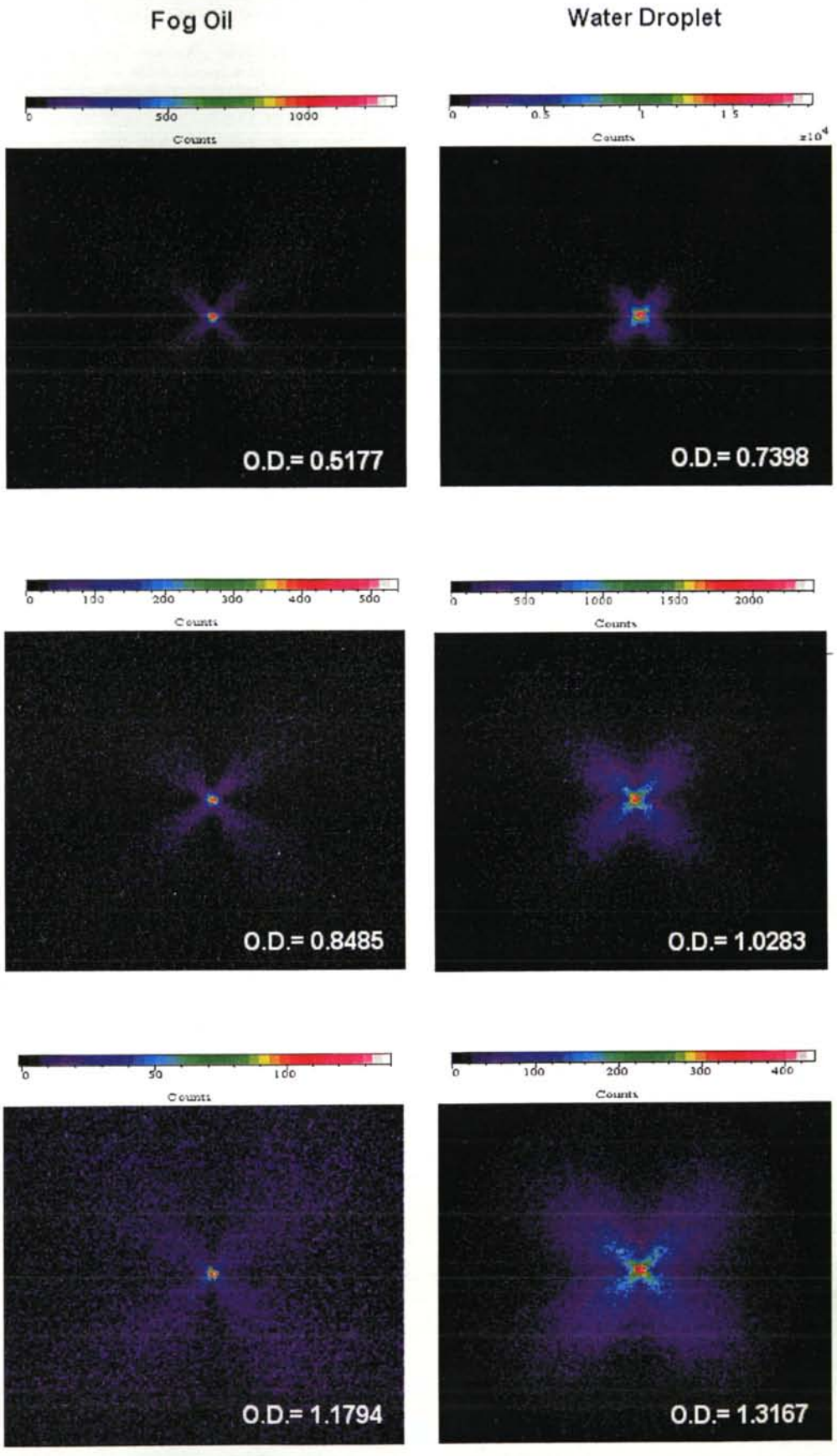


Fig. 3. Images of range-gated cross-polarized backscatter returns from, left, a fog-oil and, right, a water droplet cloud, both dispersed in a 22-m-long chamber. The gate depth is 3 m, the distance to the cloud is 100 m, and the cloud penetration distances are, left, 3.5, 6.5, and 9.5 m and, right, 6.5, 9.5, and 12.5 m.

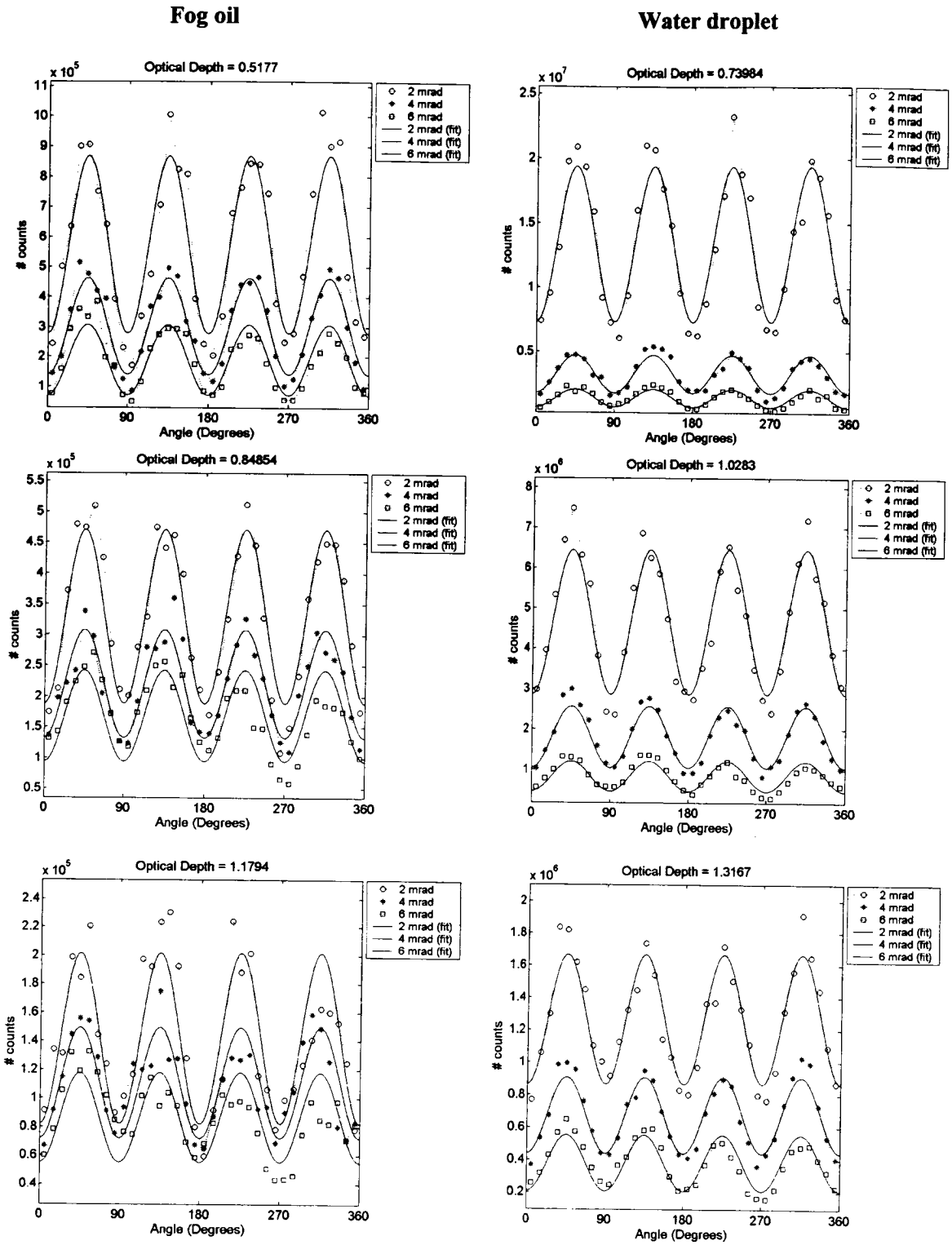


Fig. 4. Azimuthal dependence for various FOVs of the patterns shown in Fig. 3: symbols, measured pixel counts; continuous curves, best fits.

and 20, and it took about 4.2 s to complete a data-acquisition cycle. This time could be reduced with a binning pattern. In fact the two primary benefits of binning are an improved signal-to-noise ratio and the ability to increase frame rate, albeit at the expense of reduced spatial resolution.

The measurements were usually performed early in the morning so that the relative humidity was high and the wind mild. A typical measurement sequence was as follows: The conventional lidar channel was used to determine the time delay to be applied to the ICCD camera. The chamber doors

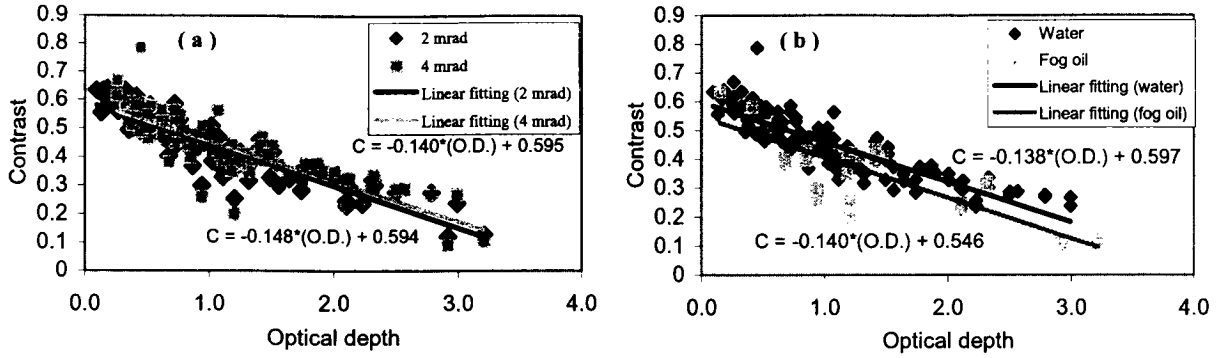


Fig. 5. Contrast values $C(\theta_i)$, Eq. (1), plotted versus optical depth for (a) FOVs of 2 and 4 mrad and (b) water and fog-oil droplets.

were closed, and the dissemination of water droplets or fog oil was started. During and for 30 s after the end of the dissemination, mixing fans were operated to ensure a good homogeneity inside the chamber. The front door was then opened, and the ICCD camera began measurements every 3 m starting at 0.5 m inside the chamber and ending at 18.5 m. The back door was opened 5 s later to allow measurement of the total optical depth. The concentration of droplets inside the chamber is assumed uniform, and the optical depth for each of the ICCD measurement is calculated as follows:

$$O.D._i = \frac{-i}{22} \ln T,$$

where $T$ is the transmission through the chamber and $i$ is the penetration distance (meters) inside the chamber. Optical depths ranging from 0.1 to 3 have been obtained.

### 3. Measurements

Before performing the measurements reported here, we characterized the laser-beam profile by imaging its effect on a canvas located 200 m from the lidar. Figure 2 shows the recorded normalized intensity as a function of FOV/2. To realize Fig. 2, we summed the charges on the CCD of each column and we normalized the result. Although 50% of the energy is contained within 0.35 mrad, it remains that 10% of the energy exceed the 2-mrad mark. This apparent broadening of the laser beam is mainly caused by imperfections of the scanner optical elements, dust on the optics, and internal reflections at the ICCD input window.

Figure 3 shows color-coded intensity images of the measured cross-polarized lidar return at different optical depths, O.D., for fog-oil (left) and water droplet (right) clouds. In this representation the radial distance of 1 pixel corresponds to 0.0476 mrad, and the intensity is normalized by the number of laser pulses summed on the ICCD chip. The images in Fig. 3 are clear reproductions of the pattern observed by Carswell and Pal,[5] but the pattern becomes smeared with increasing optical depth.

We concentrate our quantitative analysis on two particular aspects of the images in Fig. 3. First we study the azimuthal $\phi$ (Ref. 13) dependence of the cross-polarized returns $S(\theta_i, \phi)$ for a given FOV $\theta_i$. Figure 4 shows $S(\theta_i, \phi)$ as functions of $\phi$ for FOV ranges of 1.7–2.3, 3.7–4.3, and 5.7–6.3 mrad denoted by the nominal mean values $\theta_i$ of 2, 4, and 6 mrad. The plotted values are azimuthally averaged over 10 deg. Shown as continuous curves are the best fits to the equation $I = a_i \cos(4\phi) + b_i$, where $a_i$ and $b_i$ are the fit parameters for each experimental data set ($a_i < 0$ and $b_i > 0$). The cos $4\phi$ dependence and the sign of the fit parameters are that predicted by the multiple-scattering theory as discussed in Section 4.

The fit parameters are fixed so that the following condition is respected: $\Sigma|\text{fitting curve}(i) - \text{experimental data}(i)|/\Sigma|\text{experimental data}(i)| < \text{error tolerance}$, where the error-tolerance value starts at 0.1 and can increase, if necessary, up to 0.3. The typical uncertainties of the values of $a_i$ and $b_i$ are generally lower (the error tolerance is around 0.1) at 2 mrad for the small optical depths. This phenomenon could be explained by the theoretical (Monte Carlo) backscattering cross-polarization patterns obtained in Ref. 13 that show that as the concentration of the scatterers increases the patterns are located in a smaller vicinity of the point of incidence of the laser beam. In fact the contribution of the higher-order scattering events causes some blur in the pattern for the large FOVs. It thus becomes difficult to find a good fitting curve for these FOVs. The typical uncertainties in the fitting process also vary with the size of the scatterers. For the same FOV it is easier to find a fitting curve on the data for the water droplet than on the data for the fog oil because the lidar return intensity, which is highly related to the scattering phase function, is higher for the bigger particles (the water droplet in this study).

We use parameters $a_i$ and $b_i$ to calculate the contrast $(I_{\max} - I_{\min})/(I_{\max} + I_{\min})$ of the observed pattern, i.e.,

$$C(\theta_i) = \frac{-a_i}{b_i}. \quad (1)$$

The contrast values $C(\theta_i)$ are calculated for all measurements and plotted on Fig. 5 versus optical depth.

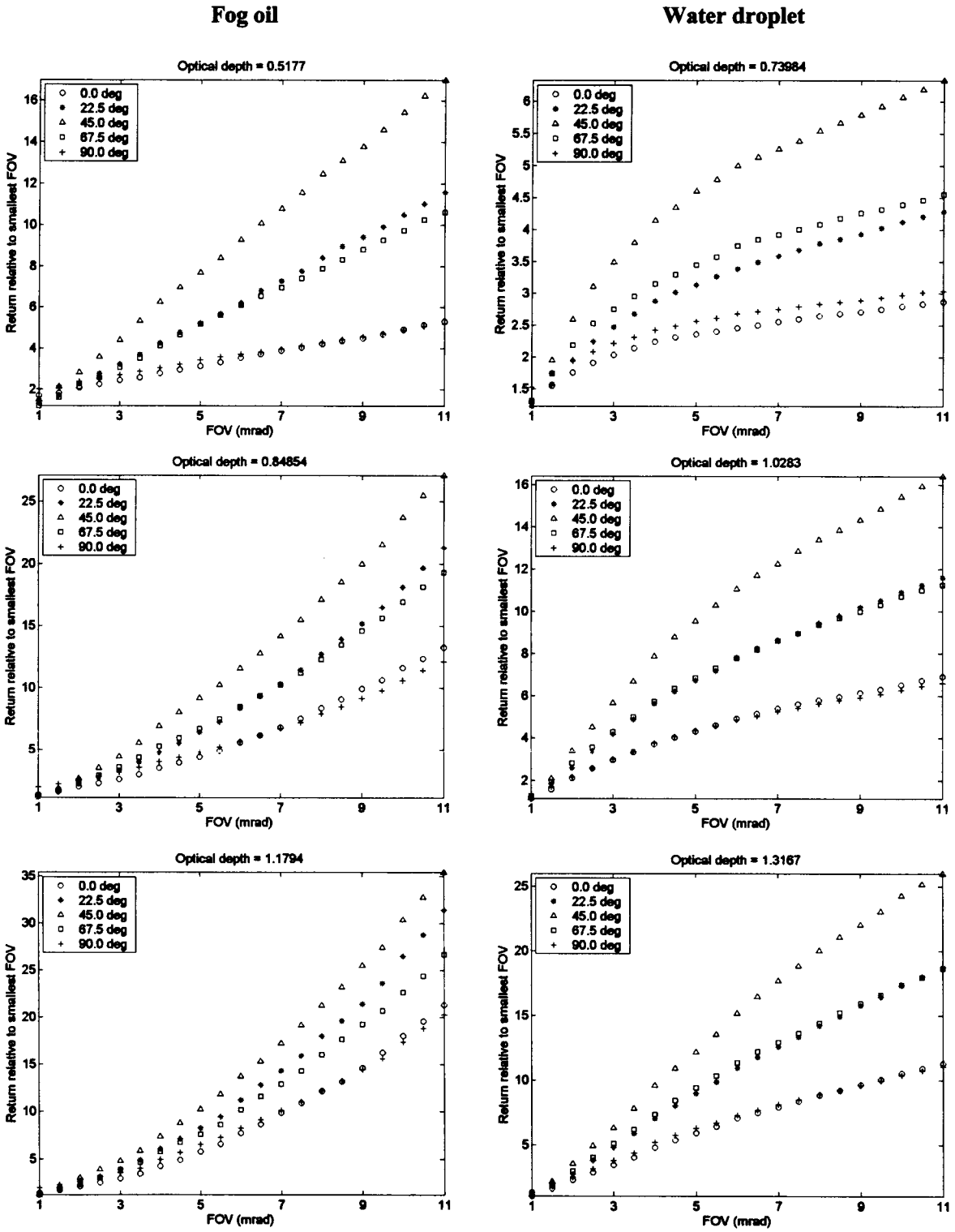


Fig. 6. Relative cross-polarized return for narrow azimuth sectors centered on 0°, 22.5°, 45°, 67.5°, and 90° plotted as functions of the FOV.

The relative dispersion of some points in Fig. 5 is probably due to the fact that the dissemination of the particles inside the aerosol chamber is not perfectly homogeneous as we assumed in calculating the optical depth (see Section 2). This must be particularly the case for fog oil because these droplets are generated only at the beginning of the aerosol chamber by a MDG Super Max 5000 fog-oil generator and are then spread over the controlled environment by a powerful electric fan that blew the air in a long (22-m) perforated plastic tube while the water droplets are generated by distributed pneumatic water nozzles.

The contrast decreases quasi-linearly with optical depth and is virtually independent of droplet size and FOV (2 and 4 mrad) if we consider that the allowed error on the fitting curve is greater than 10%. The steady contrast reduction with optical depth is attributed to higher-order scattering. Note that the generalization for larger FOVs is not shown in Fig. 5(a) because the typical uncertainties in the fitting process are high (more than 0.3) for those data. We consider that an error tolerance that is so high is too imprecise to give satisfactory results for calculation of the contrast.

The nondependence of the particle size over the linear relationship between the contrast and the optical depth can in contrast be generalized to a large particle-size range since the mean diameter for the water droplet studied was 20 μm while the geometric mean volume diameter of the fog oil was much smaller (0.8 μm).

In a second analysis we investigate the FOV(θ) dependence of the cross-polarized patterns $S(\theta, \phi_i)$ for a given azimuth angle $\phi_i$. Figure 6 shows the quantity

$$\frac{S(\theta, \phi_i)}{S(\theta = 1 \text{ mrad}, \phi_i)}$$

plotted as a function of θ for $\phi_i$ ranging from −5° to 5°, 20° to 25°, 42.5° to 47.5°, 65° to 70°, and 87.5° to 92.5° denoted by the mean values of 0°, 22.5°, 45°, 67.5°, and 90°. We observe good symmetry on both sides of 45°, indicating good radial homogeneity inside the chamber as well as good calibration of the ICCD.

#### 4. Discussion

Second- and higher-order scattering events contributing to the measured pattern $S(\theta, \phi_i)$ are schematically illustrated in Fig. 7. All recorded second-order scattering contributions with one backscattering event at $B_s$ share a common scattering plane (assuming an infinitesimal laser-beam size). By contrast the contributions of a scattering order greater than 2 also passing through $B_s$, for example, those through $T_1$ and $T_2$ in Fig. 7, all have different scattering planes. This explains why higher-order scatterings do not produce an azimuthal pattern. In this respect it is important to remember that the image of the laser beam obtained from a solid target shows that there is a fair amount of energy at large FOVs that can also create confusion in the second-order azimuthal pattern. Rakovic and Kattawar[7] have shown that the radial (FOV) and azimuthal dependence of the cross-polarized returns for second-order scattering are given by

$$I_{\perp}(\rho_s, \phi) = \beta_s{}^2 \frac{f_0(\rho_s) + f_4(\rho_s)}{4} (1 - \cos 4\phi), \quad (2)$$

where $\rho_s$ is the radial distance from the laser-beam axis, which can easily be transformed into a field of view; $\beta_s$ is the backscattering coefficient; and $f_0$ and $f_4$ are expressions involving products of two Mueller

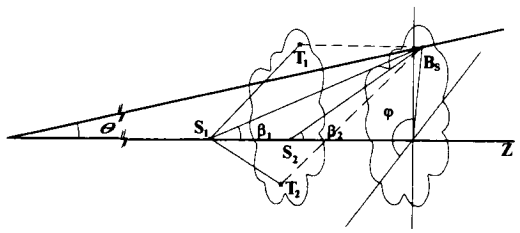


Fig. 7. Schematic representation of second- and third-order scattering contributions to lidar returns: $S_1$, $S_2$, single forward-scattering events; ϕ, azimuth angle; θ, scattering angle; $\beta_1$, $\beta_2$, backscattering angles.

matrix components integrated over all possible scattering angles for two scattering events. Using Eq. (2) in the definition of the contrast [Eq. (1)], we find that

$$C(\theta_i) = 1. \quad (3)$$

In other words the contrast in the second-order scattering cross-polarized return is constant and independent of particle size and FOV. This is consistent with our experimental observations reported in Figs. 3 and 4 except for the blurring effect of the higher-order scatterings. Moreover Eq. (2) shows that $I_{\perp}(\rho_s, 0)$ and $I_{\perp}(\rho_s, \pi/2)$ should be equal to zero. Therefore the energy recorded at these angles must come from scattering orders higher than 2. Assuming uniform intensity over ϕ for these scatterings, we approximate the contributions from the scatterings with an order of greater than 2 by averaging the image intensity over narrow azimuth sectors centered on 0°, 90°, 180°, and 270°. We calculate a different value for each FOV because it is FOV dependent. Subtracting this quantity from the full image, we obtain a result that approaches the second-order scattering pattern. We have carried out the calculations for all measurements and found a mean contrast equal to 0.95 ± 0.07 for the fog oil and water droplets at FOVs of 2, 4, and 6 mrad. This is sufficiently close to the theoretical value of 1 to be significant. The difference likely comes from a small but not negligible amount of off-axis laser-beam energy (Fig. 2).

The approximation of the uniform intensity over ϕ for the contributions of a scattering order greater than 2 must also lead to some errors. In fact these scattering orders could show some weak azimuthal patterns. However, among multiple-scattering trajectories the main contribution to the azimuthal pattern comes from near-double-scattering trajectories in which light suffers one backscattering and many near-forward scatterings. Note that subtracting $(a + b)$ from the fitted curves in Fig. 4 to match the angular dependence of the theoretical formula [Eq. (2)] would yield a contrast of exactly 1. We therefore conclude that it is relatively easy to derive with good accuracy the second-order scattering cross-polarized return from the recorded total cross-polarized return. Finally, integrating this pattern over the azimuth, we

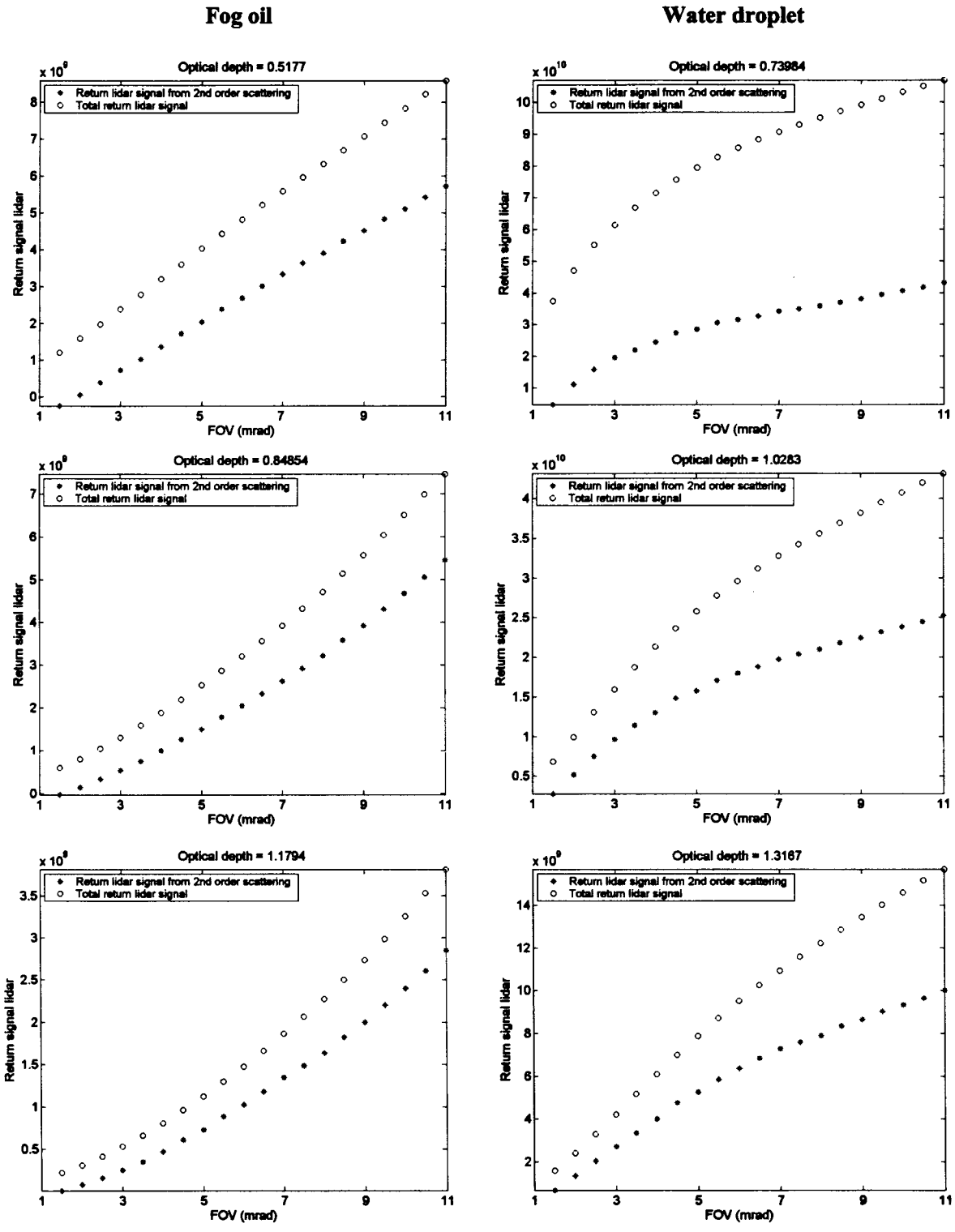


Fig. 8. Circles, total and, asterisks, derived second-order lidar returns (azimuthally integrated cross-polarized component) as functions of the FOV for the patterns displayed in Fig. 3.

obtain the FOV-dependent cross-polarized return for second-order scattering only. The interest of this transformation is that the latter quantity is amenable to analytical modeling and can thus lead to manageable retrieval techniques. In Fig. 8 we compare the second-order returns calculated as indicated above with the full returns for the recorded images of Fig. 2. These data show good similarity with the MFOV measurements reported by Roy and Bissonnette.[8]

So far, we have restricted our discussion to spherical particles for which the backscattered light at exactly 180° is not depolarized. Measurements where the same setup was used have also been performed on 1-μm glass beads and on aspherical particles such as brass flakes (0.1 μm thick and 6 μm in diameter), carbon fiber (8 μm in diameter and 3 mm long), and large (90-μm) polymeric microspheres with a calcium carbonate coating.[14] No azimuthal pattern has been observed for the three aspherical particles. In the case of the 1-μm glass beads a faded azimuthal pattern has been observed. We have attributed the fading to surface imperfections on the particles and to the presence of not perfectly spherical particles.

## 5. Conclusion

We have shown experimentally that cross-polarized lidar returns show an azimuthal dependence that is mainly caused by second-order scattering. The contrast of the azimuth features is independent of particle size and FOV and can be related to optical depth. We have also shown that, using the measured scattered light at 0° and 90° with respect to the direction of the laser-pulse polarization, we can derive the second-order-scattering pattern from the multiple-scattering pattern. This has the definite advantage of providing a measured quantity that can be directly related to tractable analytical expressions even in the presence of large multiple-scattering contributions. For example, this should greatly facilitate development of retrieval techniques for such important parameters as optical depth and particle size. However, experimentation on aspherical particles has shown the absence of the azimuthal pattern, and therefore the proposed technique appears to be limited to spherical particles.

A promising future effort is certainly the search for a theoretical expression relating the contrast of the azimuth pattern of the cross-polarized multiple-scattering return with the optical depth. In particular, as suggested by one reviewer, the combination of the contrast definition with Eq. (34) in Ref. 13 leads to an interesting equation that could be verified with the help of Monte Carlo calculation. The possibility of using other features of the azimuth patterns of lidar returns to determine microphysical parameters should also be explored further. Monte Carlo calculations such as described by Oppel and Wengenmayer[15] would be an excellent tool for this purpose. On the experimental side, planned improvements in the quality/cleanliness of the collecting and emitting optics should enhance the quality of the data. Finally there could be considerable advantages in performing simultaneous measurement of both polarization states with a single ICCD camera.

The authors thank Sylvain Cantin, Marc Grenier, and George Ménard for technical assistance. We are also indebted to S. L. Chin of Université Laval for his constant scientific support of and material contributions to this research.

## References

1. R. M. Schotland, K. Sassen, and R. J. Stone, "Observations by lidar of linear depolarization ratios by hydrometeors," J. Appl. Meteorol. **10,** 1011–1017 (1971).
2. K. Sassen, "Depolarization of laser light backscattered by artificial clouds," J. Appl. Meteorol. **13,** 923–933 (1974).
3. S. R. Pal and A. I. Carswell, "The polarization characteristics of lidar scattering from snow and ice crystals in the atmosphere," J. Appl. Meteorol. **16,** 70–80 (1977).
4. C. M. R. Platt, "Lidar observation of a mixed-phase altostratus cloud," J. Appl. Meteorol. **16,** 339–345 (1977).
5. A. I. Carswell and S. R. Pal, "Polarization anisotropy in lidar multiple scattering from clouds," Appl. Opt. **19,** 4123–4126 (1980).
6. S. R. Pal and A. I. Carswell, "Polarization anisotropy in lidar multiple scattering from atmospheric clouds," Appl. Opt. **24,** 3464–3471 (1985).
7. M. J. Rakovic and G. W. Kattawar, "Theoretical analysis of polarization patterns from incoherent backscattering of light," Appl. Opt. **37,** 3333–3338 (1998).
8. G. Roy, L. R. Bissonnette, C. Bastille, and G. Vallée, "Retrieval of droplet-size density distribution from multiple-field-of-view cross-polarized lidar signals," Appl. Opt. **38,** 5202–5211 (1999).
9. L. R. Bissonnette, G. Roy, L. Poutier, S. G. Cober, and G. A. Isaac, "Multiple-scattering lidar retrieval method: tests on Monte Carlo simulations and comparisons with *in situ* measurements," Appl. Opt. **41,** 6307–6324 (2002).
10. G. Roy, L. Bissonnette, and C. Bastille, "Efficient field-of-view control for multiple-field-of-view lidar receivers," in *Proceedings of 19th International Laser Radar Conference*, NASA/CP-1998-207671/PT1 (U.S. GPO, Washington, D.C., 1998), pp. 767–770.
11. Y. Saito, M. Ishizuka, S. Nagao, T. D. Kawahara, A. Nomura, and K. Noguchi, "Imaging of multiple scattered laser beam passing through clouds: experiment and computer simulation," in *Proceedings of 19th International Laser Radar Conference*, NASA/CP-1998-207671/PT1 (U.S. GPO, Washington, D.C., 1998), pp. 169–172.
12. C. Buil, *CCD Astronomy: Construction of an Astronomical CCD Camera* (Willmann-Bell, Richmond, Va., 1991), pp. 252–259.
13. M. J. Rakovic, G. W. Kattawar, M. Mehrübeoglu, B. D. Cameron, L. V. Wang, S. Rastegar, and G. L. Coté, "Light backscattering polarization patterns from turbid media: theory and experiment," Appl. Opt. **38,** 3399–3408 (1999).
14. G. Roy, L. R. Bissonnette, C. Bastille, and G. Vallée, "Estimation of cloud droplet size density distribution from multiple-field-of-view lidar returns," Opt. Eng. **36,** 3404–3415 (1997).
15. U. G. Oppel and M. Wengenmayer, "Diffusion of the lidar beam seen from the receiver," in *Lidar Multiple Scattering Experiments*, C. Werner, U. G. Oppel, and T. Rother, eds., Proc. SPIE **5059,** 21–30 (2003).

#521703

CA024186